Energy 315 (2025) 134455

Contents lists available at ScienceDirect

Energy

journal homepage: www.elsevier.com/locate/energy

Nitrogen sources and formation routes of nitric oxide from pure ammonia combustion

Xiangtao Liu [a], Jicang Si [b,**], Guochang Wang [c], Mengwei Wu [b], Jianchun Mi [a,b,*]

[a] College of Engineering, Peking University, Beijing, 100871, PR China
[b] Marine Engineering College, Dalian Maritime University, Dalian, 116026, PR China
[c] State Key Laboratory of Clean and Efficient Coal Utilization, Taiyuan University of Technology, Taiyuan, 030024, PR China

ARTICLE INFO

Keywords:
Ammonia combustion
MILD combustion
NO formation
Thermal-NO
Fuel-NO

ABSTRACT

This study is to investigate firstly the nitrogen sources and formation routes of nitric oxide (NO) from pure ammonia combustion. A well stirred reactor (WSR) is used for chemical processes while a jet-in-hot-coflow (JHC) configuration of ammonia flames is employed to account for the flow impact. Different combustion regimes are simulated by changing various parameters in both WSR and JHC cases. Results reveal that the production of thermal-NO increases with T_{WSR} (WSR working temperature) at $T_{WSR} \geq$ 1900–2500 K, below which it is negligible. In contrast, the fuel-NO exhibits a non-monotonic behavior with T_{WSR}: initially increasing, then decreasing, and eventually increasing again. Interestingly, it is found that reactions within the Extended Zeldovich route play a crucial role in reducing the fuel-NO. The simulated JHC flames of pure ammonia indicate that MILD combustion minimizes both fuel- and thermal-NO emissions. Furthermore, the fuel-NO always emerges as the dominant source of NO, no matter which combustion regime occurs. The thermal-NO however remains negligible in pure ammonia combustion except in those cases of enriched-oxygen and extremely-high ambient temperatures.

1. Introduction

To mitigate the greenhouse effect caused by fossil fuel combustion, alternative energy sources have been being explored to reduce CO_2 emissions, the most detrimental greenhouse gas [1]. Sustainable energy sources, such as wind, solar, and tidal power, face challenges due to high storage costs and intermittent availability [2]. As a result, zero-carbon fuels like hydrogen and ammonia have gained global attention as alternative fuels. Ammonia offers significant advantages over hydrogen, including much lower costs of storage and transportation, and fewer safety risks during combustion [3].

However, traditional ammonia combustion faces significant challenges, including difficult ignition, unstable flames, and high NO_x emissions [4]. Various attempts have been made to address these issues. Effective strategies to enhance the flammability of ammonia include blending it with more flammable substances, such as hydrocarbons [5] and hydrogen [6], as well as increasing the oxygen content of reactants through a process known as oxygen-enriched combustion [7]. Nonetheless, these methods are likely to elevate combustion temperature and thus thermal-NO_x emissions. In contrast, combustion in fuel-rich [8] and H_2O-diluted environments [9], as well as pressured conditions [10], has proven effective in reducing NO_x emissions. However, these approaches may lead also to reduced combustion efficiency and/or instability. Staged combustion [11] and plasma [12] technologies have been shown to enhance the stability of NH_3 combustion while reducing NO_x emissions. On the other hand, the complexity of their design and operation limits their practical application.

Among these methods, the moderate or intense low-oxygen dilution (MILD) combustion is a promising solution for addressing the challenges against the ammonia combustion [13]. Numerous studies on MILD combustion of hydrocarbon fuels have demonstrated its key characteristics, including a large reaction zone, uniform temperature and species distribution, an indistinct flame front, and ultra-low NO_x emissions [14]. More importantly, MILD combustion can achieve a significantly higher average temperature within the combustor compared to traditional combustion (TC), despite having lower temperature peaks [15]. This characteristic helps to avoid combustion instability and facilitates the use of low calorific value fuels [16], such as ammonia.

* Corresponding author. College of Engineering, Peking University, Beijing 100871, PR China.
** Corresponding author.
E-mail addresses: sjc@dlmu.edu.cn (J. Si), jmi@pku.edu.cn (J. Mi).

https://doi.org/10.1016/j.energy.2025.134455
Received 27 October 2024; Received in revised form 30 November 2024; Accepted 6 January 2025
Available online 7 January 2025

In recent years, several studies have been published on ammonia MILD combustion. Sorrentino et al. [17] experimentally demonstrated the feasibility of pure ammonia MILD combustion in a cyclone combustor, showing that it produced significantly lower NO_x emissions than traditional combustion. Similarly, Xie et al. [18] found that the MILD technique effectively reduces NO_x emissions from ammonia combustion, due to the enhanced reduction of NO production. Liu et al. [19] conducted a numerical investigation of a one-dimensional premixed laminar ammonia flame under various combustion regimes, revealing that MILD combustion exhibits a greater flame thickness, slower flame propagation, and milder heat release reactions with far lower NO emissions than does the traditional combustion. Examining the influence of oxygen concentration in a semi-industrial scale furnace, Cafiero et al. [20] found that, at a fixed power rate, the stabilization of MILD combustion can be established when the inlet oxygen concentration (X_{O2}) is 4 % higher than for the traditional combustion. Additionally, while reducing the slip of NH_3, an increase of X_{O2} also raises NO_x emissions; a balance can be achieved at $X_{O2} = 37$ %, yielding the lowest overall NO_x emissions. Recently, Wang et al. [21] conducted a comparative study on the ammonia and methane flames. They concluded that the ammonia combustion exhibits lower peak temperature and heat release, as well as a larger reaction zone, more likely to establish the MILD combustion. However, even under the MILD regime, more NO_x still results from ammonia than methane combustion, especially under fuel-lean conditions. To further reduce NO_x emissions from ammonia combustion, it is crucial to clarify the formation routes of NO_x and the source of their N atoms.

In pure ammonia combustion, NO_x can be categorized into two types based on the origin of N: i.e., fuel-NO_x and thermal-NO_x [22]. Thermal-NO_x forms through the oxidation of N_2 present in air/oxidant or diluents, whereas N atoms in fuel-NO_x originates from the N-containing fuels, specifically from NH_3 in pure ammonia combustion. Identifying the N source of NO_x in combustion is crucial for guiding research efforts and targeting effective NO_x reduction strategies. The assumption is favorable that NO_x emissions in ammonia combustion are predominantly composed of fuel-NO_x [23]. However, the quantitative analysis is lacking due to the challenge of separating the two types of NO_x.

Zhao et al. [24] addressed this challenge by substituting N_2 in the diluent with a non-reactive fictitious gas (FN_2) to isolate fuel-NO. Although this approach effectively quantifies the fuel-NO, it has notable limitations. In practical combustion scenarios, N_2 in the oxidant suppresses the conversion of NH_3 to N_2 while promoting the formation of NO, which does not occur with FN_2. Li et al. [25] attempted to separate the fuel- and thermal-NO_x by combusting H_2 and NH_3 separately to achieve the same flame temperature, assuming that the thermal-NO_x produced under identical temperatures would be identical. The difference in NO_x emissions would then be attributed to the oxidation of nitrogen atoms in NH_3 (fuel-NO_x). However, achieving the same combustion temperature for both fuels is operationally difficult, and factors such as varying radical concentrations and degrees of dilution can influence thermal-NO_x formation, which are not accounted for in their method. Another widely used approach is to categorize reactions involved in NO production and consumption into distinct routes. In this framework, NO produced through reactions associated with the Extended Zeldovich route is classified as the thermal-NO, while NO formed via other reactions is considered as the fuel-NO [26]. While effective for hydrocarbon fuel combustion [27], this method encounters difficulties when applying to ammonia combustion. Recent findings of Liu et al. [28] indicate that the Extended Zeldovich route significantly contributes to the NO consumption, leading to a negative concentration of the thermal-NO, which is clearly unreasonable. This suggests that the conventional method is unsuitable for ammonia combustion, necessitating an explanation of this phenomenon and potential improvements. Wu et al. [29] recently introduced the method of marking N atoms to decouple thermal- and fuel-NO_x. This technique is both accurate and effective. However, it has so far been limited to simulations involving ammonia/diesel-fueled engines, leaving the N sources of NO_x in pure ammonia combustion being unexplored under different combustion regimes.

To fill this gap in research, the present numerical study is designated to investigate the N sources and formation routes of NO_x in pure ammonia combustion under various conditions. Specifically, the N-atom marking method is employed to distinguish between various N sources for NO_x. Moreover, the study systematically uses different parameters such as inlet temperature, oxygen concentration, equivalence ratio, ignition conditions, and combustion regimes. The specific objectives of this study are twofold:

1) To disclose the N sources and formation mechanisms of NO_x in pure ammonia combustion under a wide range of conditions.
2) To explain the negative contribution of the Extended Zeldovich route to the NO formation, found previously.

2. Computational approach

2.1. Computational configurations

This numerical study employs a combination of zero-dimensional (0-D) and two-dimensional (2-D) simulations. Firstly, the concentrations of thermal-NO and fuel-NO, along with their generation mechanisms, are investigated in a 0-D well-stirred reactor (WSR) for the premixed NH_3/O_2/N_2 combustion. Then, the N sources of NO across different combustion regimes and technologies are analyzed in a 2-D jet-in-hot-coflow (JHC) configuration, which accounts for flow dynamics and more accurately represents actual flame conditions.

In WSR, the reactants are perfectly mixed prior to the reactions, allowing for an exclusive focus on the chemical processes while neglecting flow and mixing effects. This ideal model is suitable for investigating the mechanisms of NO production and consumption. Here, the volume (V), pressure (P), and residence time (τ) of the WSR are maintained at 76 cm^3, 1 atm, and 1 s, respectively, aligning with parameters used in our previous study [28] to ensure consistency. The inlet flow rate can be calculated using $M_{in} = \rho V/\tau$, where ρ is the density of the gas mixture within the reactor. Additionally, the inlet oxygen concentration (X_{O2}), temperature (T_{in}), and equivalence ratio (Φ) of the inlet reactants are varied to investigate the NO mechanisms under different conditions and combustion regimes.

While the WSR combustion is effective for studying chemical mechanisms, practical combustion involves significant effects from flow and mixing, which are critical for establishing and characterizing various flames under different combustion regimes [30]. Therefore, it is essential to account for these factors to further explore the proportions of thermal-NO and fuel-NO in pure ammonia combustion. It has been demonstrated that varying ignition and coflow conditions within an open JHC configuration with a bluff-body can establish various combustion regimes, including traditional combustion and MILD combustion, without altering the burner design [31]. Accordingly, this study simulates a bluff-body JHC configuration to investigate NO sources under different combustion regimes and technologies. Specifically, for the validation, the experimental bluff-body burner of Kariuki et al. [32] is employed, consisting of a hollow cylinder with a diameter of 35 mm and a conical bluff-body with a 90° cone angle. The bluff-body, featuring a maximum diameter of $d = 25$ mm, is secured by a coaxial rod with a diameter of 6.35 mm. Of note, Kariuki et al. [32] stabilized a CH_4/air flame in stationary ambient air. A schematic of the JHC configuration is presented in Fig. 1(a), while the detailed boundary conditions for both experiments and simulations are provided in Table 1.

For the present simulation (SIM) cases, the boundary conditions are modified to facilitate the investigation of ammonia combustion. Firstly, the reactants were replaced with NH_3/air. Additionally, to establish different combustion regimes, the external ambient air is replaced with a slow (1 m/s) hot coflow comprised of the complete combustion products

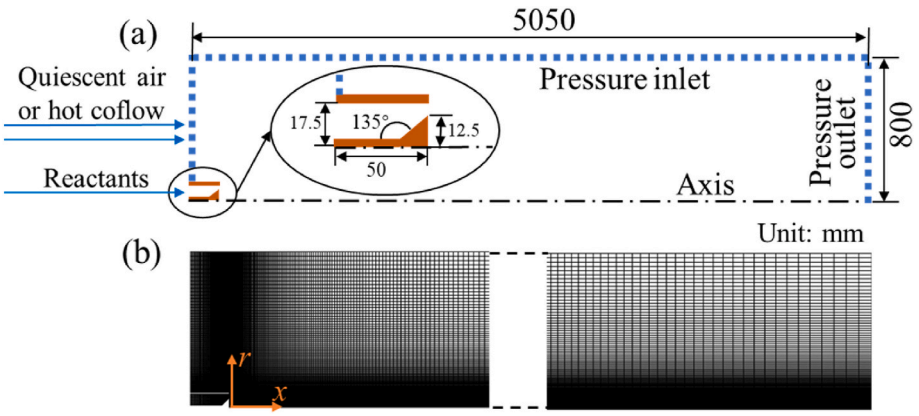

Fig. 1. (a) Schematic of the computational domain and (b) the mesh for the JHC configuration.

Table 1
Boundary conditions for experiment (EXP) [32] and simulation (SIM) cases[a].

Cases	Jet			Coflow				
	Reactants	U_J (m/s)	Φ_J	U_C (m/s)	T_C (K)	$X_{O2,C}$ (%)	$X_{N2,C}$ (%)	$X_{H2O,C}$ (%)
EXP	CH_4/air	21.6	0.75	0	300	21	79	0
SIM	NH_3/air	5.47	1.0	1.0	500–2000	0	68.9	31.1

[a] U_J = the jet velocity, Φ_J = the equivalence ratio, U_C = the coflow velocity, T_C = the coflow temperature, $X_{i,C}$ = the volume concentration of the ith specie in the coflow.

of the inlet reactants. For all simulation JHC cases, the inlet velocity is set to 5.47 m/s with an equivalence ratio of $\Phi = 1.0$. The ignition conditions and coflow temperature (T_C) are adjusted to achieve various combustion regimes and technologies, specifically traditional, flameless, MILD, and high-temperature combustion. Furthermore, the sources of NO from pure ammonia JHC flames under pressured and oxygen-enriched combustion technologies are also calculated to ensure the comprehensiveness of the study. Relevant details are summarized in Tables 1 and 4.

Given the axisymmetric nature of the JHC system, 2-D computational domains and meshes are utilized to reduce the computational cost of the Reynolds-averaged Navier-Stokes (RANS) simulations [33]. To evaluate grid independence, three orthogonal structured grids are employed, consisting of 28,600, 58,800, and 114,600 cells, respectively, for simulating the experimental case. The results obtained from the grids with 58,800 and 114,600 cells show only minor differences, while significant variations are observed with the 28,600-cell grid. Therefore, the grid comprising 58,800 cells is selected for modeling the bluff-body JHC in this study. The mesh configuration is illustrated in Fig. 1(b).

2.2. Atom marking method

To differentiate between fuel- and thermal-NO, this study employs the atom marking method. In brief, this approach involves marking the N atoms in the reactants while ensuring that the physical properties and chemical reactions of the species remain unchanged before and after marking. For example, the N atom in N_2 in the reactant is marked as N*. Following combustion, all NO containing the marked N* atoms is identified as the thermal-N*O originating from N_2, while the remaining unmarked NO is classified as the fuel-NO, arising from the oxidation of NH_3. The method is implemented by modifying the chemical reaction mechanism. The net reaction rates of all species are preserved before and after the modification. For species that do not contain nitrogen atoms, such as O_2, the rates of production and consumption remain unchanged after the modification. For nitrogen-containing species, such as NH, the combined production rates of N*H and NH after the modification are equivalent to the original NH production rate, and the same applies to the consumption rates. The implementation details of this method can be found in Refs. [29,34] and will not be elaborated here.

2.3. Computational models

The 0-D WSR computations are presently conducted using the CHEMKIN-Pro software [35]. The chemical reactions are modeled with a modified version of the Zhang-2021 detailed kinetic mechanism. The original Zhang-2021 mechanism [36] comprises 38 species and 263 reactions, and is suitable for modeling pure ammonia and NH_3/H_2 combustion over a wide range of temperatures, pressures, and equivalence ratios. To distinguish between fuel- and thermal-NO, the species and reactions involving nitrogen atoms were modified. The resulting mechanism expands to 72 species and 869 reactions, with the parameters for species and reactions derived from the original Zhang-2021 mechanism.

The 2-D JHC calculations are performed using ANSYS Fluent. For the NH_3/air JHC flames analyzed in this study, the modified Zhang-2021 mechanism is applied to model the reactions and identify the sources of NO. As for the CH_4/air flames used in the experimental validation, the chemical reactions are calculated using the GRI-2.11 [37] kinetic mechanism, whose accuracy in simulating methane combustion has been repeatedly validated [38,39]. In addition, some CFD models are employed to ensure accurate predictions. Specifically, turbulence is modeled using the standard k-ε model, with the model constant $C_{1\varepsilon}$ adjusted to 1.7 [31] to improve the representation of the round bluff-body burner. The interaction between turbulence and chemistry is captured using the model of eddy dissipation concept (EDC), which has been extensively verified and widely adopted in previous numerical studies, e.g., Refs. [16,40]. The EDC model assumes that all chemical reactions occur in the regions where turbulent kinetic energy is dissipated. The residence time scale of species in these regions is calculated as $\tau = C_\tau(\nu/\varepsilon)^{0.5}$, where C_τ is the time scale constant. In combustion simulations, using the default values of C_τ often results in overestimations of combustion temperature and ignition performance [15, 41]. To address this, the time scale constant in this study is set to C_τ = 0.82, as recommended by Parente et al. [42]. Radiation effects are

modeled with the discrete ordinates (DO) model [43], coupled with the weighted sum of gray gases (WSGG) model. Additionally, the in-situ adaptive tabulation (ISAT) method [44] is employed to accelerate computations, with an ISAT error tolerance set to 10^{-5}. The convergence criteria are residuals below 10^{-6} for energy and radiation intensity equations and 10^{-5} for other equations.

3. Validations of computational methods

The validation of the computational approach used in this study involves three components: the Zhang-2021 mechanism, the N atom marking method, and the CFD models applied in the JHC simulations. The accuracy of the Zhang-2021 mechanism has been extensively validated in previous studies for both 0-D [36] and 2-D [45] simulations. Consequently, this validation is not repeated here.

The N atom marking method is validated by comparing the evolution of temperature, NO, N_2O, and NO_2 in the WSR for the oxidation of marked NH_3, marked N_2, marked NH_3 & N_2, and unmarked reactants, with inlet conditions set at $T_{in} = 1200$ K & $X_{O2} = 6$ %, $T_{in} = 1600$ K & $X_{O2} = 6$ %, and $T_{in} = 1200$ K & $X_{O2} = 21$ %. The results are shown in Fig. 2, along with the relative error (E) in the maximum values of temperature, NO, N_2O, and NO_2. The temperature and NO_x profiles across

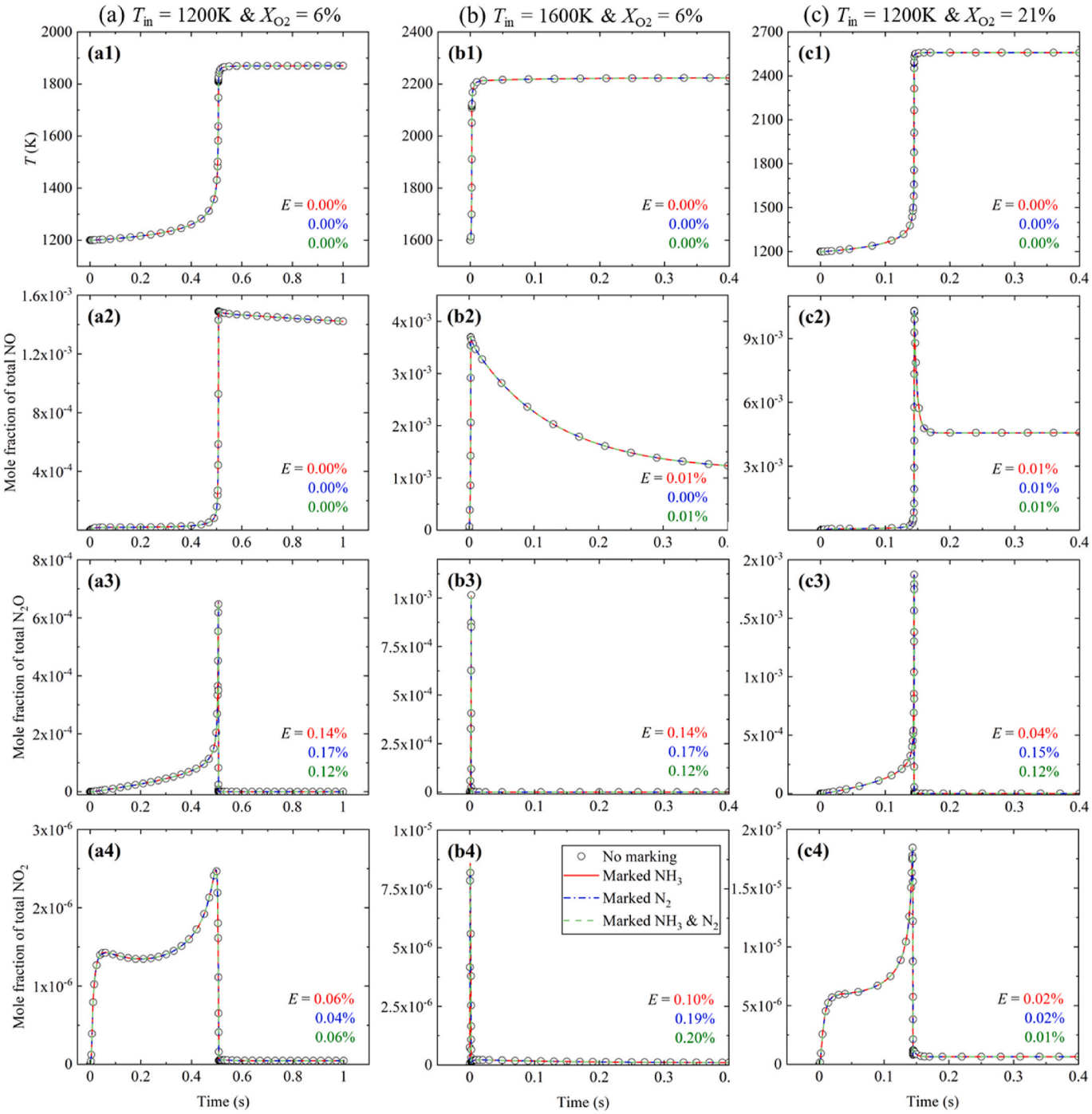

Fig. 2. Evolutions of temperature, NO, N_2O and NO_2 in WSR from the oxidation of marked and unmarked reactants at (a) $T_{in} = 1200$ K & $X_{O2} = 6$ %, (b) $T_{in} = 1600$ K & $X_{O2} = 6$ %, and (c) $T_{in} = 1200$ K & $X_{O2} = 21$ %. On the plots, E denotes the relative error of the maximum values, with red, blue, and green representing cases of marked NH_3, marked N_2, and marked NH_3 & N_2, respectively.

the different cases show excellent agreement, with E less than 0.2 %, which are negligible. The slight error may be attributed to the increased number of species in the modified mechanism, which enhances the chemical stiffness of the simulation [46]. This error decreases with higher computational precision, supporting this conjecture.

Overall, the marking method demonstrates strong accuracy and is suitable for subsequent calculations focusing on temperature and NO_x. Fig. 2 also indicates that, in ammonia combustion, NO_x primarily consists of NO, while N_2O and NO_2 are present in negligible amounts. This finding aligns with previous studies [26,28]. Therefore, subsequent analyses focus exclusively on NO. Additionally, the results show that chemical reactions reach a steady state within 1 s, confirming the appropriateness of using a residence time of $\tau = 1$ s for the WSR calculations.

To verify the accuracy of the CFD models used in the JHC simulations, Fig. 3 compares the predicted and measured axial velocity (U_x), radial velocity (U_y), and normalized concentration of OH ($X_{OH}/X_{OH,max}$) at $x/d = 0.4$, 0.8, 1.2, and 1.6 in the CH_4/air jet flame, where X_{OH} is the local OH concentration and $X_{OH,max}$ is its maximum value. The experimental results are obtained from the measurements by Kariuki et al. [32]. Obviously, the CFD results closely match the trend of the experimental data and show good quantitative agreement with the measurements, despite some minor discrepancies. This confirms that the CFD models used are suitable for the subsequent 2-D JHC flame simulations.

4. Chemical analysis on thermal- and fuel-NO mechanisms

In this section, the ideal WSR model is applied to calculate pure chemical reactions of the $NH_3/N_2/O_2$ mixture under different conditions. Fig. 4 shows the concentrations of thermal-NO and fuel-NO, the proportion of fuel-NO to total NO, and the WSR working temperature (T_{WSR}) as functions of T_{in} using the oxidant of $X_{O2} = 6$ % (left) and air (right) at $\Phi = 0.5$, 1.0, and 2.0. Different vertical scales are used for cases with different Φ. Various combustion regimes are realized and labeled in the figure. The criteria for classifying combustion regimes, proposed by Liu et al. [28], are listed in Table 2, where X_{NOx} represents the concentration of NO_x, T_{ai} denotes the auto-ignition temperature, and ΔT (= T_{WSR} - T_{in}) is the calculated temperature rise.

Fig. 4(a1-a3) illustrates that MILD combustion mainly occurs under the dilute conditions of $X_{O2} = 6$ %. In the premixed NH_3/air combustion cases, MILD combustion is limited to the fuel-rich combustion within a very narrow range of T_{in} (see Fig. 4(b3)). Unlike other combustion regimes, the MILD combustion does not produce the thermal-NO. It is also shown that the concentrations of both fuel-NO ($X_{Fuel\text{-}NO}$) and thermal-NO ($X_{Thermal\text{-}NO}$) decrease as Φ increases, a trend that will be further analyzed in Fig. 7. Additionally, the proportion of fuel-NO to total NO ($P_{Fuel\text{-}NO} = X_{Fuel\text{-}NO}/X_{Total\text{-}NO}$) rises with increasing Φ for both dilute and air cases. This occurs because N atoms in the fuel-NO originate from NH_3, and as Φ increases, the global concentration of NH_3 grows, thus enhancing $X_{Fuel\text{-}NO}$ and raising its contribution to $X_{Total\text{-}NO}$.

Fig. 4 demonstrates that, regardless of Φ and X_{O2}, the thermal-NO appears only at $T_{WSR} > 1900$–2500K. This finding is not consistent with the results previously reported by Sabia et al. [47], where thermal-NO was assumed to form once the temperature reached 1600 K. This discrepancy suggests that previous studies may have overestimated the contribution of thermal-NO. Besides, It is shown that $X_{Thermal\text{-}NO}$ increases with further increasing T_{WSR} and T_{in}, as is expected [48]. In contrast, $X_{Fuel\text{-}NO}$ initially increases, then decreases with increasing T_{in}, followed by a gradual rise. Furthermore, the increase in T_{in} leads to a rapid decrease in $P_{Fuel\text{-}NO}$ due to the combined effects of reduced fuel-NO and increased thermal-NO. Interestingly, under both diluted and air conditions, $X_{Fuel\text{-}NO}$ drops mildly, while its proportion decreases sharply, at greatly lower values of T_{in} for the stoichiometric case ($\Phi = 1$) than for both the rich and lean cases. This is because, overall, a higher T_{WSR} results from $\Phi = 1$ at the same T_{in}.

In order to investigate the reasons for the non-monotonic trend of fuel-NO with T_{in}, we choose the four cases of $T_{in} = 300$ K, 660 K, 1400 K, and 2500 K for $\Phi = 1.0$. Note that the locally maximal and minimal

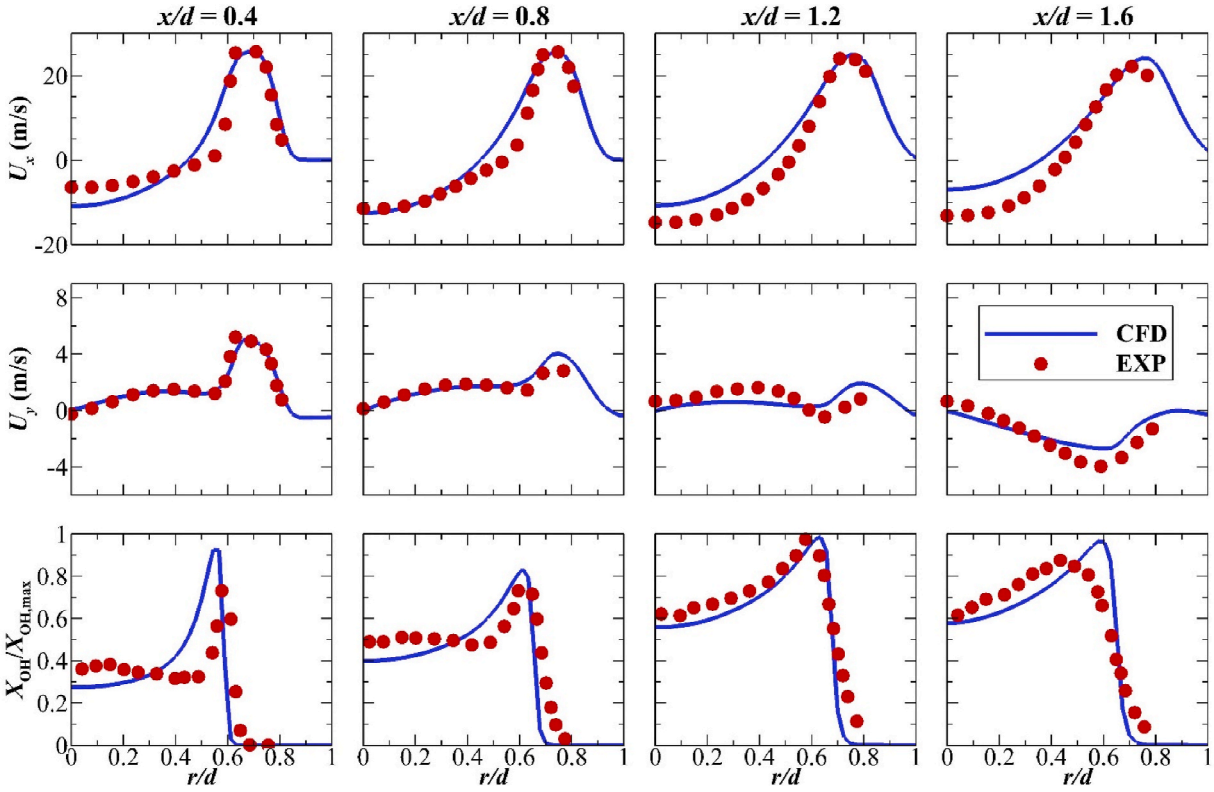

Fig. 3. Comparison of the measured (EXP) [32] and calculated (CFD) distributions of the axial velocity (U_x), radial velocity (U_y), and normalized concentration of OH ($X_{OH}/X_{OH,max}$) for the combustion from JHC configuration at $x = 0.4d$, $0.8d$, $1.2d$, and $1.6d$.

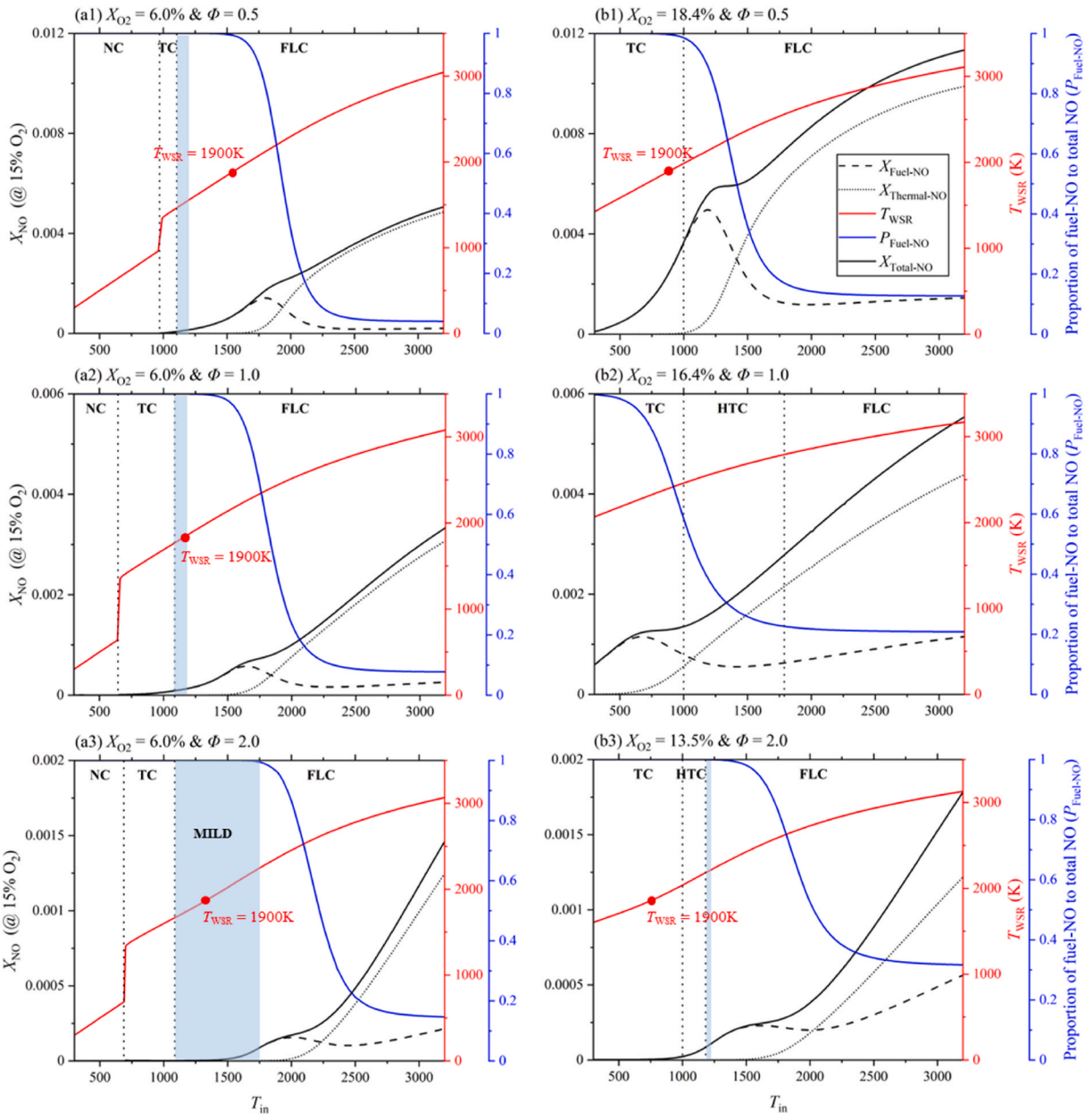

Fig. 4. Concentrations of thermal- and fuel-NO ($X_{Thermal-NO}$, $X_{Fuel-NO}$), along with the proportion ($P_{Fuel-NO}$) of $X_{Fuel-NO}$ to total NO ($X_{Total-NO}$) and the WSR working temperature (T_{WSR}), versus the inlet temperature (T_{in}) for Φ = 0.5 (top), 1.0 (mid) and 2.0 (bottom). Combustion cases: (a) diluted (X_{O2} = 6 %, left) and (b) air (right). On the plots, NC = no combustion; TC = traditional combustion; HTC = high temperature combustion; FLC = flameless combustion; MILD = moderate or intense low-oxygen dilution.

Table 2
Classification of different regimes for the combustion of $NH_3/N_2/O_2$.

Combustion regime	Inlet conditions	Working conditions
Traditional combustion (TC)	$T_{in} < T_{ai}$	$\Delta T > T_{ai}$
High temperature combustion (HTC)	$T_{in} > T_{ai}$	$\Delta T > T_{ai}$
Flameless combustion (FLC) generally	$T_{in} > T_{ai}$	$\Delta T < T_{ai}$
MILD combustion specifically	$T_{in} > T_{ai}$	$\Delta T < T_{ai}$ & $X_{NOx} \leq 100$ ppm

values of $X_{Fuel-NO}$ occur at $T_{in} \approx 660$ K and 1400 K. In these cases, the fuel-NO production rates are calculated for the top 10 related reactions. The results are displayed in Fig. 5. Herein, the N atoms in the gas N_2 are marked by the symbol *. Thus, all the marked N atoms are derived from the oxidant N_2, and the corresponding thermal-NO is expressed as N*O. Similarly, all unmarked N atoms are from the fuel NH_3, and thus the fuel-NO is simply written as NO. The main reactions associated with fuel-NO and thermal-N*O are listed in Table 3.

Fig. 5 indicates that as T_{in} rises from 300 K to 660 K, reactions R2, R3, and R12 are enhanced, leading to an increase in NO production, particularly through the HNO route. When T_{in} is further increased to 1400 K, reactions R1 and R2 associated with HNO weaken, resulting in reduced NO production. Simultaneously, the increase in temperature facilitates the decomposition of N^*_2 into N* atoms within the combustion system, thereby enhancing reaction R8, which contributes to the reduction of fuel-NO. These factors combined cause the rise in T_{in} to decrease the fuel-NO. When T_{in} is increased from 1400 K to 2500 K, the significance of reaction R6 diminishes. Meanwhile, the rise in

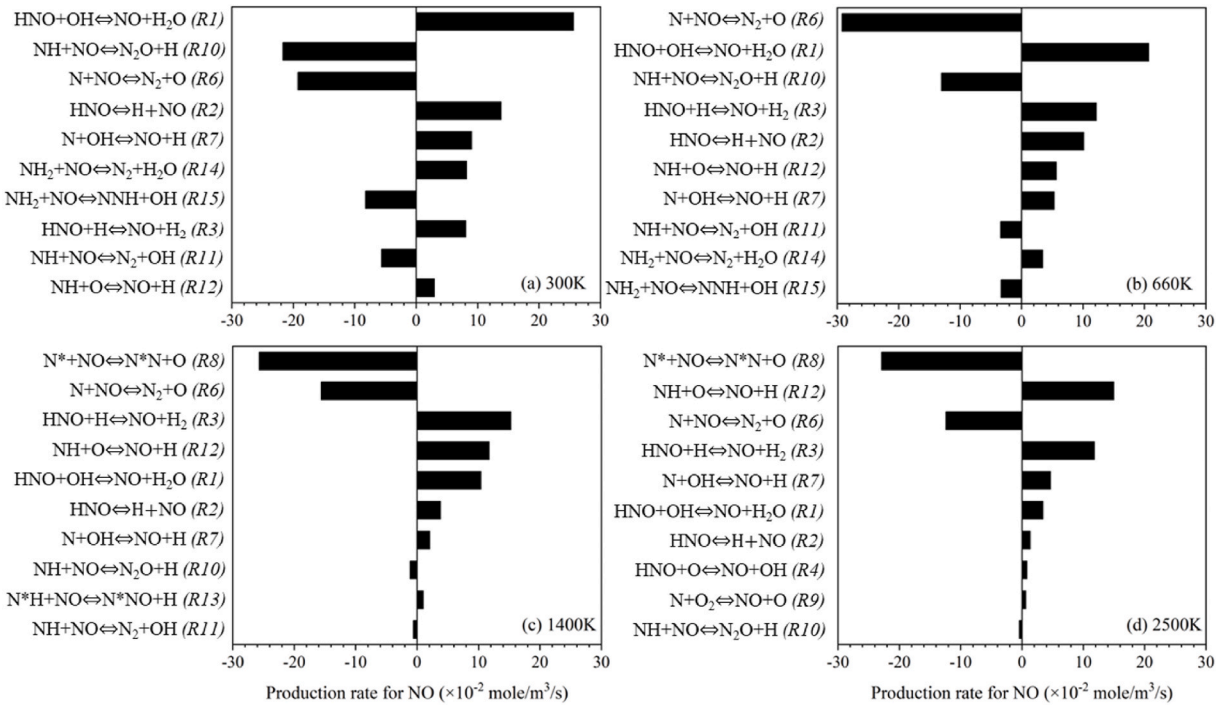

Fig. 5. Fuel-NO production rates for the top 10 reactions of the WSR combustion of NH_3/air at $X_{O2} = 16.4$ % and $\Phi = 1.0$: (a) $T_{in} = 300$ K, (b) 660 K, (c) 1400 K, and (d) 2500 K.

Table 3
Major fuel- and thermal-NO related reactions in ammonia combustion.

Fuel-NO related reactions		Thermal-N*O related reactions	
R1	HNO + OH ⇔ NO + H_2O	**R16**	HN*O ⇔ H + N*O
R2	HNO ⇔ H + NO	**R17**	N*+N*O=N*$_2$+O
R3	HNO + H ⇔ NO + H_2	**R18**	N + N*O ⇔ N*N + O
R4	HNO + O ⇔ NO + OH	**R19**	N*+OH ⇔ N*O + H
R5	HNO + O_2⇔NO + HO_2	**R20**	N*+O_2⇔N*O + O
R6	N + NO ⇔ N_2+O	**R21**	NH + N*O ⇔ N*NO + H
R7	N + OH ⇔ NO + H	**R22**	NH + N*O ⇔ N*N + OH
R8	N*+NO ⇔ N*N + O	**R23**	N*H + N*O ⇔ N*$_2$O + H
R9	N + O_2⇔NO + O	**R24**	N*H + N*O ⇔ N*$_2$+OH
R10	NH + NO ⇔ N_2O + H	**R25**	NH_2+N*O ⇔ N*N + H_2O
R11	NH + NO ⇔ N_2+OH	**R26**	NH_2+N*O ⇔ N*NH + OH
R12	NH + O ⇔ NO + H	**R27**	N*NH + O ⇔ NH + N*O
R13	N*H + NO ⇔ N*NO + H	**R28**	N*N*H + O ⇔ N*H + N*O
R14	NH_2+NO ⇔ N_2+H2O	**R29**	N*O_2+H ⇔ N*O + OH
R15	NH_2+NO ⇔ NNH + OH	**R30**	N*O + O ⇔ N*O_2

Table 4
Conditions for the present JHC calculations.

Cases		Ignition	Pressure (atm)	$X_{O2,J}$ (%)	T_C (K)	E_{NO} (ppm)	E_{N*O} (ppm)
1	TC	✓	1	16.4	500	528.16	0.00
2	HTC	✓	1	16.4	1050	532.30	0.00
3	MC	×	1	16.4	1500	82.15	0.07
4	FLC	×	1	16.4	2000	119.69	22.80
5	TC-Pressured combustion	✓	10	16.4	500	238.11	0.06
6	TC-Oxygen-enriched combustion	✓	1	30.0	500	642.71	198.58

temperature promotes the decomposition of O_2 into O atoms, which boosts the NO production rate via reaction R12. Based on the above analysis, the non-monotonic trend of $X_{Fuel\text{-}NO}$ with T_{in} can be understood.

It is worth noting that in the original studies [49,50], reactions R6-R9 were categorized under the Extended Zeldovich route (also known as the thermal route), traditionally viewed as the pathway for producing thermal-N*O. However, the results shown in Fig. 5 reveal that these reactions play a significant role in reducing fuel-NO, especially R6 and R8. When T_{in} = 1400 K, approximately 94.2 % of the fuel-NO consumption occurs via these two reactions. As T_{in} is further increased to 2500 K, their contribution to fuel-NO consumption rises further, reaching 97.1 %. This phenomenon led to the previous calculation mistakenly assuming that the concentration of thermal-NO was negative [28]. The present calculation explains this implausibility successfully. More significantly, it is demonstrated that the assumption of the Extended Zeldovich path exclusively producing the thermal-NO is incorrect for ammonia combustion. Consequently, the criteria for classifying NO reaction pathways need to be revised, which deserves further investigation in future studies.

To analyze the variation of thermal-N*O with the inlet temperature (T_{in}), Fig. 6 depicts the N*O production rates for the top 10 related reactions at T_{in} = 800 K, 1400 K and 2500 K with $X_{O2} = 16.4$ % and Φ = 1.0. Note that the horizontal coordinate for the case of T_{in} = 800 K is different from the other cases. Regardless of T_{in}, R17 and R18 remain to dominate in producing and consuming N*O, respectively. As T_{in} increases from 800 K to 1400 K, the increase in working temperature significantly boosts the rates of both reactions, resulting in higher N*O levels. As T_{in} rises further to 2500 K, the increased production of N* and O atoms reduces the efficiency of N*O formation via R17 and its consumption via R18. Interestingly, the difference in N*O produced and consumed by these two reactions remains similar to that at 1400 K. However, a marked enhancement in R19 increases N*O production, driven by the higher N* concentration, causing the N*O concentration to rise with T_{in}, as depicted in Fig. 4.

To explore the mechanisms of NO and N*O productions at different Φ, Fig. 7 presents the production rates for the top 10 related reactions in NH_3/air combustion at Φ = 0.5, 1.0 and 2.0. The inlet temperature is set at T_{in} = 2000 K to ensure that significant levels of NO and N*O are detectable for analysis, even under fuel-rich conditions.

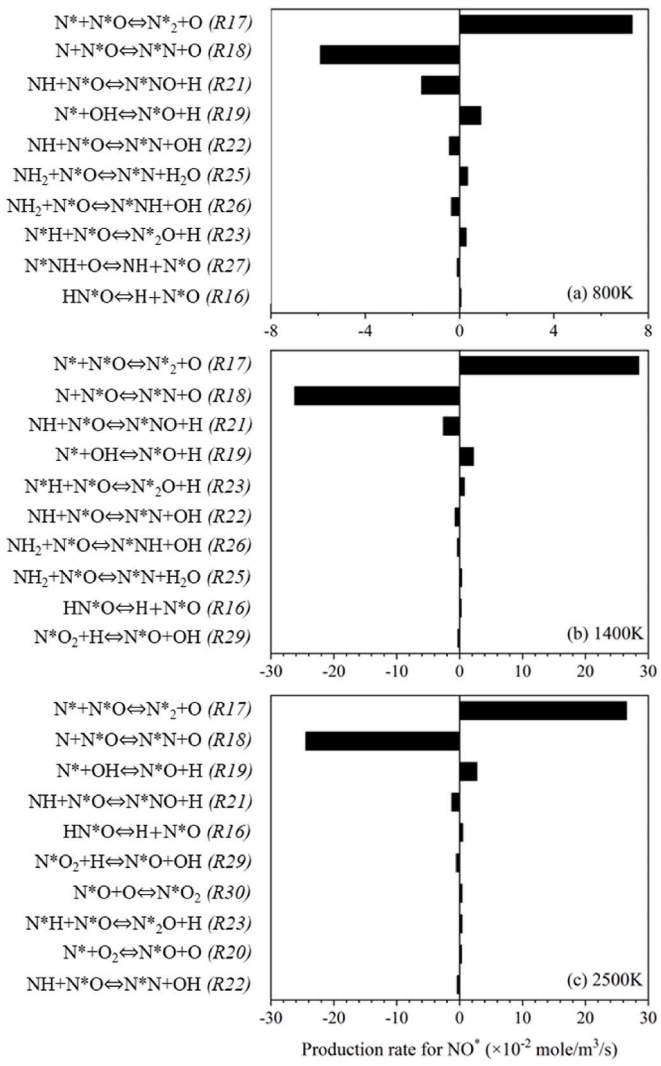

Fig. 6. Thermal-N*O production rates for the top 10 related reactions of the WSR combustion of NH_3/air at $X_{O2} = 16.4$ % and $\Phi = 1.0$: (a) $T_{in} = 800$ K, (b) 1400 K, and (c) 2500 K.

Overall, those reactions associated with fuel-NO show higher rates at $\Phi = 2$. This is because the fuel-NO comes from the oxidation of NH_3, and as Φ increases, the concentration of NH_3 in the reactants increases, boosting reactions associated with fuel-NO. Additionally, more N atoms are produced with increasing inlet NH_3, significantly enhancing the reaction rates of R6 and R7. At the same time, the concentration of O atoms decreases [51], resulting in a lower rate for R12 than under stoichiometric and fuel-lean conditions. Conversely, under fuel-lean conditions, the scarcity of N atoms reduces the significance of R6, making NO consumption less favorable than in $\Phi = 1$ and 2 conditions.

As for the thermal-N*O, it is mainly controlled by R17 and R18, with R17 being the main N*O-producing reaction and R18 dominating its consumption. Overall, the reaction rates for both reactions are highest at $\Phi = 1$ and lowest at $\Phi = 0.5$. This trend occurs because the thermal-N*O is highly sensitive to temperature, and $\Phi = 1$ corresponds to the highest T_{WSR}, while $\Phi = 0.5$ has the lowest. In addition, under the fuel-rich condition at $\Phi = 2$, the abundant N atoms enhance R18, which leads to a reaction rate that surpasses that of R17, resulting in less thermal-N*O, as shown in Fig. 4. In contrast, the low concentration of N atom in the fuel-lean case causes a significantly lower reaction rate for R18 compared to R17, yielding a higher N*O concentration than those observed for $\Phi = 1$ and 2.

To investigate the oxidation mechanisms of ammonia and nitrogen at different Φ and their interactions, Fig. 8 presents the major oxidation pathways for the WSR combustion of NH_3/air at $T_{in} = 2000$ K and $\Phi = 0.5$, 1.0 and 2.0. In this analysis, nitrogen atoms in N_2 are marked so that all marked N* atoms originate from N_2 molecules, while unmarked N atoms are derived from NH_3. It is important to note that this pathway primarily highlights the behavior of N and N* atoms. Reactions that do not involve nitrogen species, such as the decomposition of H_2 by OH, one of the major consumers of OH radicals [52], are not included in Fig. 8.

Overall, the main oxidation pathways under different Φ are similar, with some minor differences. For the oxidation of N^*_2, the specie N*N*H plays a role under the fuel-lean condition at $\Phi = 0.5$, while N^*H_2 becomes relatively important under the fuel-rich condition at $\Phi = 2.0$. Regarding the oxidation pathway of NH_3, notable differences arise when comparing the fuel-lean ($\Phi = 0.5$) condition to the stoichiometric ($\Phi = 1.0$) and fuel-rich ($\Phi = 2.0$) conditions. Firstly, N_2O can be neglected in the conversion of NO to N_2 at $\Phi = 0.5$, which results from the weakened R10. Additionally, the oxidation path N ← NO is reversed compared to the stoichiometric and fuel-rich conditions. This change is attributed to the weakened R7 due to the low concentration of N atoms, and the enhanced R9 due to the higher concentration of O_2. The reaction rates mentioned above can be referenced from Fig. 7. In contrast, under the fuel-rich condition, low inlet oxygen concentration leads to weakened reactions involving O and O_2. Therefore, at $\Phi = 2.0$, the pathways $NH_2 \rightarrow NH \rightarrow HNO \rightarrow NO$ and $N \rightarrow NO$ occur with O and O_2 playing a minor role, unlike in the fuel-lean and stoichiometric cases. More importantly, Fig. 8 illustrates that, regardless of Φ, the oxidations of N_2 and NH_3 are coupled via semi marked NN*O and N*N, with the latter being the most dominant, formed by reactions R8 and R18.

5. Thermal and fuel-nitric-oxides from pure ammonia JHC combustion

In this section, the effects of flow and mixing are taken into account to examine the proportion of thermal nitric-oxide (NO) and fuel-NO in a practical setting through the simulation of the bluff-body JHC configuration. To ensure a comprehensive analysis, different combustion regimes are simulated, including traditional combustion (TC), high-temperature combustion (HTC), flameless combustion (FLC), and its sub-regime MILD combustion [16,28]. The different regimes are established by varying ignition and coflow temperature conditions, as specified in cases 1–4 of Table 4. The table also includes the information on pressure, oxygen concentrations of the jet ($X_{O2,J}$), and emissions of NO_x. According to our calculations, in the JHC cases, NO emerges as the primary contributor to NO_x emissions, while the emissions of both N_2O and NO_2 are more than three orders of magnitude lower than that of NO. This observation aligns with the previous study on JHC flames [45]. Consequently, this section focuses exclusively on the emissions of fuel-NO (E_{NO}) and thermal-N*O (E_{N^*O}).

In these simulations, "ignition" refers to initializing a small region ($0 < x/d < 2.5$, $0 < r/d < 0.9$) at 2500 K before combustion reactions begin. E_{NO} and E_{N^*O} refer to the emissions of NO and N*O generated within the reaction zone, measured at the end of the reaction zone (RZ), as illustrated in Fig. 9(a). According to Rashed et al. [53], the boundary of the RZ is defined by the contour $R_H = X_H/X_{H,max} = 0.01$, where X_H is the mole fraction of H, and $X_{H,max}$ is its maximum values in the computational domain. However, for MILD and FLC, where the reaction zone extends beyond the calculation domain, the results at the end of the computational domain are used as an approximation.

Fig. 9 depicts the contours of the volume fractions of fuel-NO and thermal-N*O, along with the field temperature of the NH_3/air JHC flames under different combustion regimes at $\Phi = 1.0$. The maximum concentrations of NO ($X_{NO,max}$) and N*O ($X_{N^*O,max}$) in the computational domain, as well as the maximum temperature (T_{max}) are also displayed on the plots. First, let us check whether the different combustion regimes are successfully established. The criteria for classifying the combustion regimes are listed in Table 2. For JHC configuration, the temperature

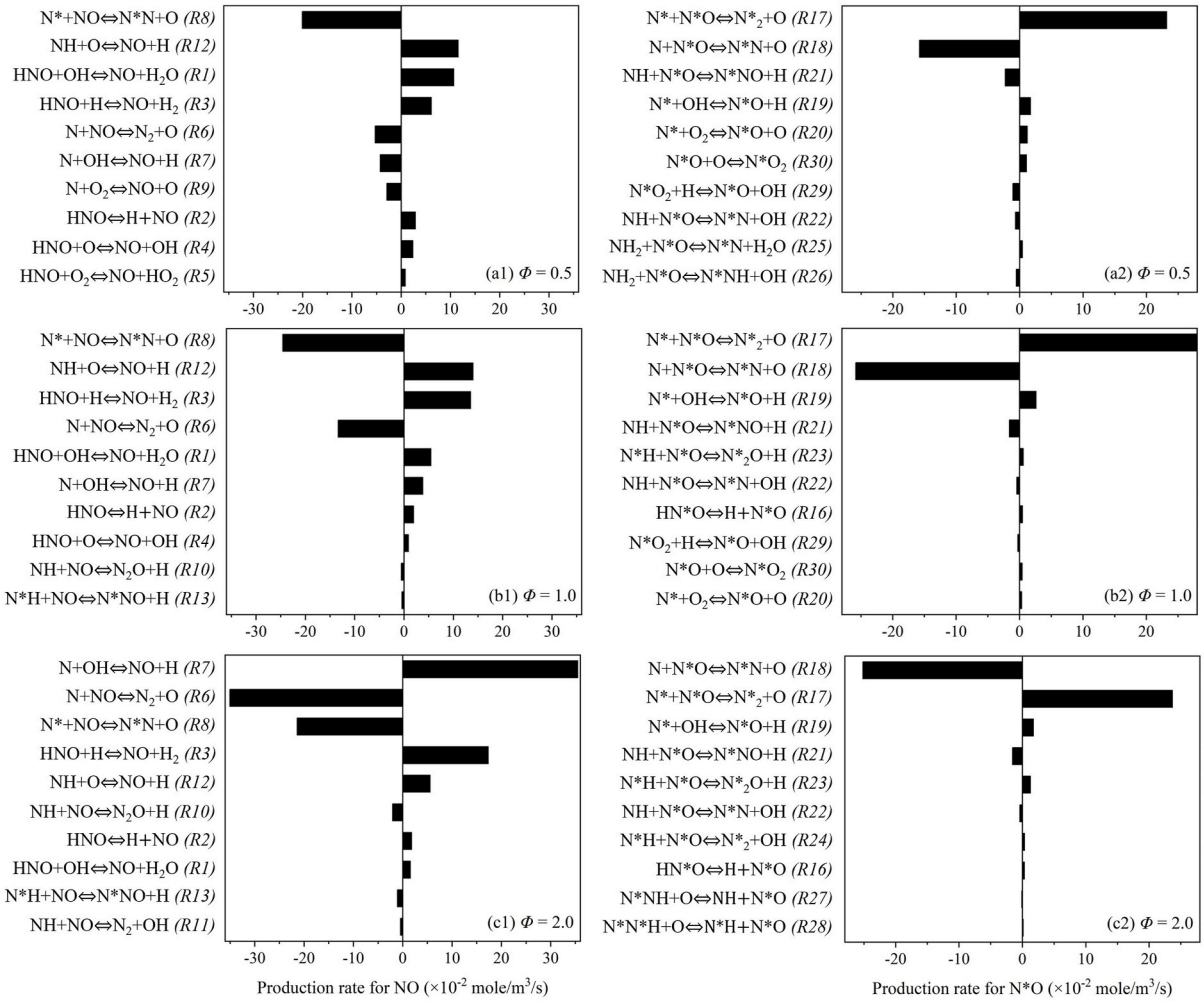

Fig. 7. Fuel-NO (left) and thermal-N*O (right) production rates for the top 10 related reactions for the WSR combustion of NH_3/air at T_{in} = 2000 K: (a) Φ = 0.5, (b) 1.0 and (c) 2.0.

rise is calculated as $\Delta T = T_{max} - T_C$, and the auto-ignition temperature (T_{ai}) of the flame ($X_{O2,J}$ = 16.4 %) is 1000 K (±5 K), determined using the same method as Liu et al. [28]. In Case 1, where T_C is lower than T_{ai} and ΔT = 1103 K exceeds T_{ai}, the condition is suitable for the traditional combustion (TC). For Case 2, both T_C and ΔT are higher than T_{ai}, establishing the high-temperature combustion (HTC). Cases 3 and 4 satisfy the conditions for flameless combustion (FLC), as T_C is greater than T_{ai} and ΔT is below T_{ai}. However, Case 3, which has NO_x emissions below 100 ppm, falls into the sub-regime of FLC, i.e., MILD combustion; with its NO_x emissions up to 315.8 ppm, Case 4 corresponds to conventional FLC. Overall, the different combustion regimes are well established according to the specified criteria.

Interestingly, despite identical inlet conditions, combustion behaviors in JHC and WSR exhibit notable differences. For instance, under the conditions of Case 3, where T_C = 1500 K, $X_{O2,J}$ = 16.4 %, and Φ = 1.0, the JHC achieves a maximum temperature of T_{max} = 1651 K, with the emissions of E_{NO} = 82.15 ppm and E_{N^*O} = 0.07 ppm. This case is categorized as MILD combustion regime. In contrast, the WSR combustion under the same conditions (T_{in} = 1500 K, X_{O2} = 16.4 %, and Φ = 1.0) reaches a significantly higher working temperature (T_{WSR} = 2686 K), and is classified as HTC regime. Furthermore, the corresponding emissions of fuel-NO and thermal-N*O are markedly higher, measured at 1861 ppm and 5341 ppm, respectively. These differences arise because the WSR assumes uniform spatial distributions of species and reactions, making it a valuable tool for analyzing chemical reactions at specific spatial points within an actual combustion chamber. In contrast, real combustion systems such as the JHC are influenced by factors like flow, mixing, and dilution. Consequently, the distributions of reactions and heat release in the JHC are non-uniform, and the reactant concentrations at reaction sites differ from those at the inlets. This highlights the necessity of conducting JHC simulations in this study to capture these realistic combustion and emission characteristics.

Fig. 9 illustrates that in TC and HTC, the flames attach to the rear of the bluff-body, while in MILD combustion (MC) and FLC, the flames are more dispersed throughout the computational domain, necessitating different horizontal and vertical coordinate scales. Across all combustion regimes, the fuel-NO and thermal-N*O are mainly concentrated in regions with elevated temperatures, indicating their direct dependence on temperature [54]. Among the four regimes, MILD combustion exhibits the lowest peak temperatures, as well as the lowest peak concentrations of both fuel-NO and thermal-N*O. Additionally, Table 4 shows that MC results in the lowest NO emissions, highlighting its advantage in reducing NO_x emissions. In contrast, FLC presents the highest thermal-NO emissions among Cases 1–4 due to the extremely high temperatures in the coflow, which generate substantial amounts of N*O in the downstream region. This indicates that elevated ambient temperatures should be avoided to minimize N*O emissions. However, FLC has lower peak fuel-NO concentrations and emissions compared to TC and HTC. This reduction can be attributed to two factors: the lower peak temperatures in FLC; and the extended residence time of reactants

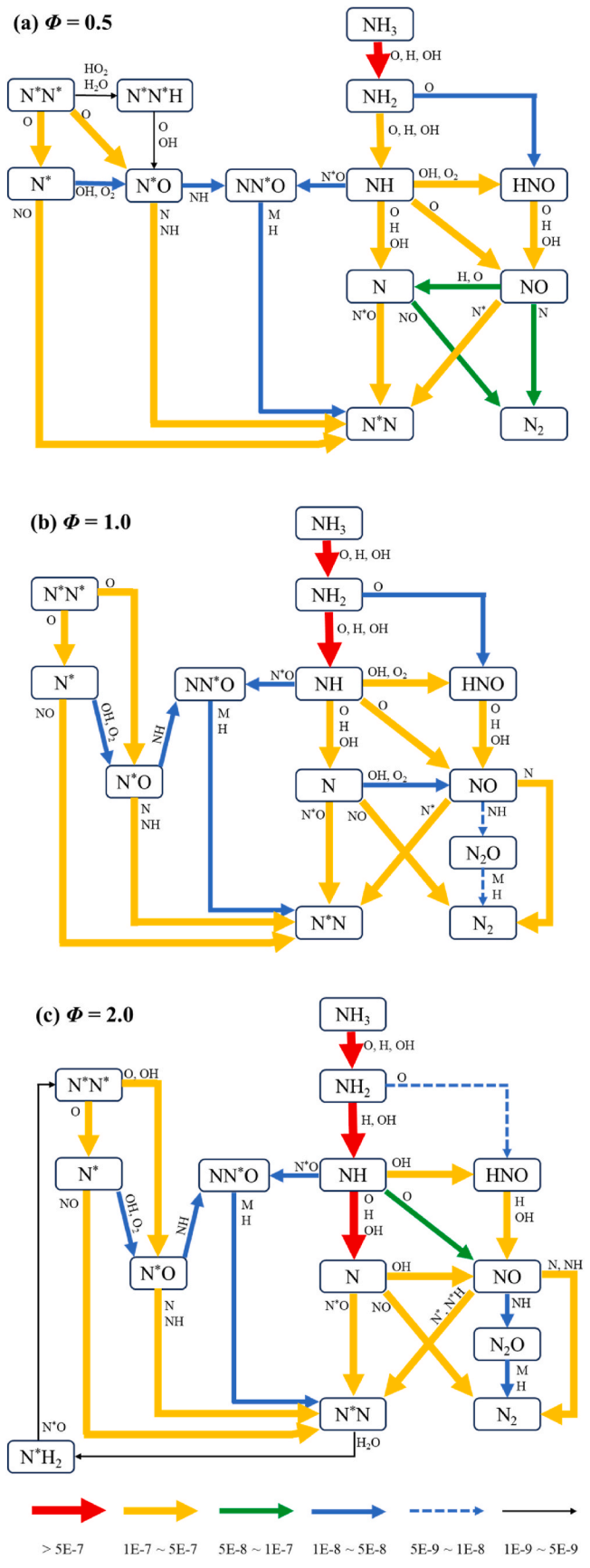

Fig. 8. Major NH_3 oxidation pathways for the WSR combustion of NH_3/air at T_{in} = 2000 K: (a) Φ = 0.5, (b) 1.0 and (c) 2.0.

at high temperatures in TC and HTC due to the recirculation zone behind the bluff-body, which promotes fuel-NO formation. Overall, MC and FLC significantly reduce total emission of nitrogen oxides, making them preferable options for ammonia combustion.

It is worth pointing out that, except for FLC with extremely high T_C, thermal-N*O is negligible in other combustion regimes, where the maximal concentrations are below 3 ppm. This suggests that, in pure ammonia combustion, thermal-N*O generally plays a minimal and negligible role, except under extremely-high temperature conditions, which are uncommon in practical combustion applications. To validate this observation, the pressured and oxygen-enriched JHC flames of pure ammonia under the TC regime are simulated, as these technologies are considered promising for enhancing ammonia combustion. Besides, both approaches result in higher combustion temperatures, which could potentially increase thermal-N*O production, making it essential to evaluate their impact. These two technologies are tested using traditional combustion (TC) as a baseline. Pressured combustion involves raising the working pressure from 1.0 atm to 10 atm, while the oxygen-enriched combustion increases the oxygen concentration in the jet ($X_{O2,J}$) from 16.4 % to 30 %. The conditions for these simulations are outlined in cases 5 and 6 of Table 4, with the results presented in Fig. 10.

For the pressured and oxygen-enriched flames, the auto-ignition temperatures are 910 K (±5 K) and 965 K (±5 K), respectively. Given that $T_C < T_{ai}$ and $\Delta T > T_{ai}$ for both cases, they are categorized as traditional combustion, the most common regime for these technologies. The results indicate that the pressured and oxygen-enriched flames exhibit higher combustion temperatures and corresponding thermal-N*O peaks compared to the normal TC in case 1. In the pressured flame, although $X_{N*O,max}$ is relatively high, the overall thermal-N*O emissions are very low and can be considered negligible. Interestingly, despite the elevated peak temperature, the pressured flame shows significantly lower fuel-NO peaks and emissions than the normal TC; this deserves a further investigation. In contrast, the oxygen-enriched flame, with its higher combustion temperature, leads to E_{N*O} reaching 198.58 ppm, the highest value among cases 1–6. It also exhibits the highest fuel-NO concentrations and emissions of the six cases examined.

From these analyses, a clear conclusion emerges: in pure ammonia combustion, the fuel-NO is the predominant NO source, while the thermal-N*O remains negligible except in those cases involving oxygen-enriched combustion or extremely high ambient temperatures in combustion. Consequently, the classification of the Extended Zeldovich route in pure NH_3 combustion may need to be optimized to emphasize its role in consuming fuel-NO, which will be the focus of our future research.

6. Conclusions

This study has numerically investigated the N sources and mechanisms of nitric-oxide (NO) production in pure ammonia combustion under various combustion regimes, employing the N atom marking method to differentiate between the fuel-NO and thermal-NO productions. The analysis began with a systematic examination of the NO formation sources and mechanisms under different equivalence ratios, inlet oxygen concentrations, inlet temperatures (T_{in}), and combustion regimes in a 0-D well-stirred reactor (WSR). Subsequently, considering the effects of flow and mixing, a 2-D bluff-body JHC configuration was used to explore the NO emissions from traditional, high-temperature, MILD, and flameless combustion regimes. Additionally, a comprehensive investigation was ensured by the CFD simulations of pressured and oxygen-enriched JHC flames of pure ammonia under traditional combustion. The key findings, based on the results reported in Sections 4 and 5, can be summarized below:

(1) In the pure ammonia combustion, the thermal-NO is produced only at combustion temperatures exceeding 1900 K, and its concentration increases with higher T_{in}. The fuel-NO, on the

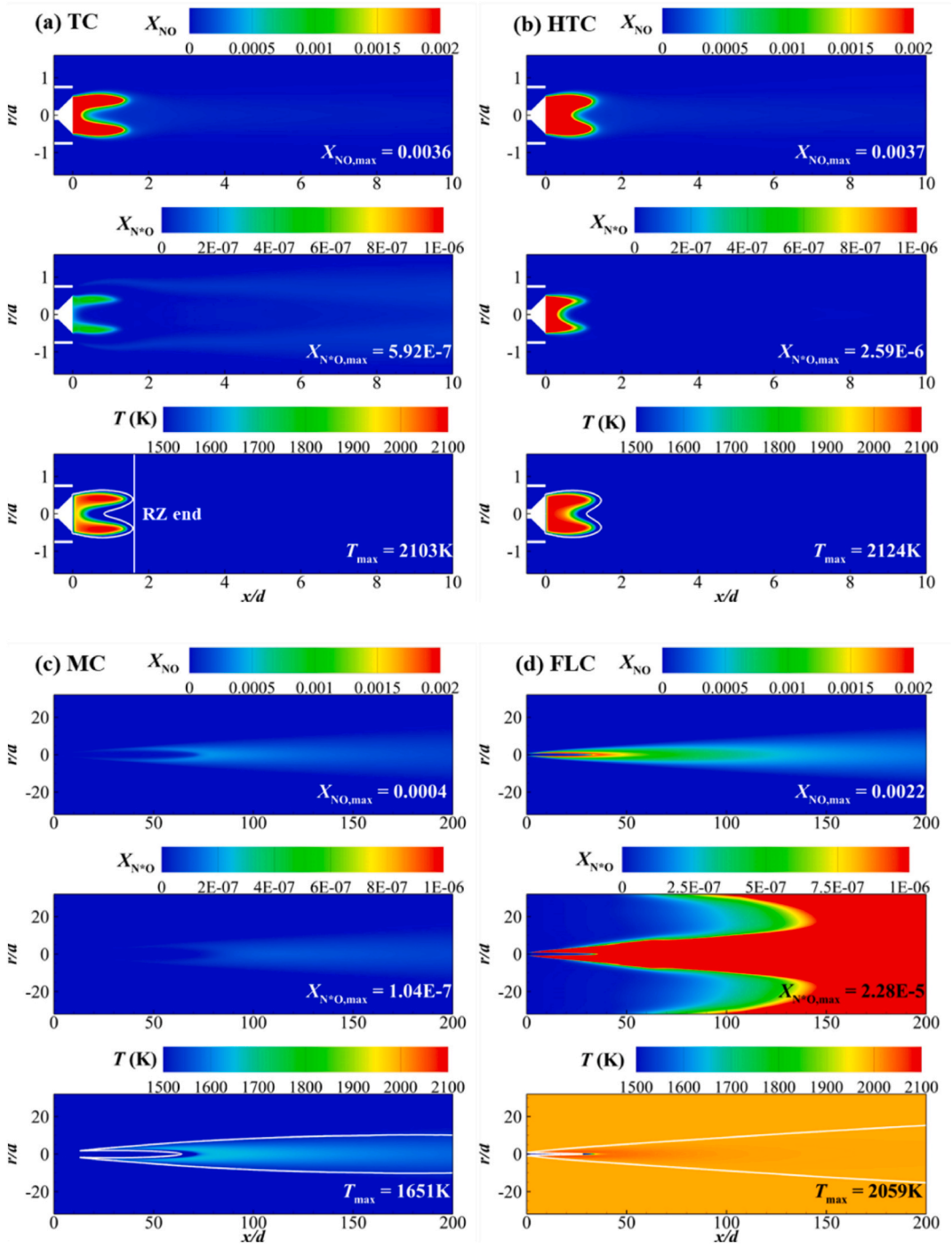

Fig. 9. Contours of the volume fractions of NO and N*O, along with the temperature field for the NH_3/air JHC flames at $\Phi = 1.0$ under different combustion regimes of (a) TC, (b) HTC, (c) MC and (d) FLC. On the plots, TC = traditional combustion; HTC = high temperature combustion; MC = MILD combustion; FLC = flameless combustion. White lines represent the RZ boundaries.

other hand, shows a non-monotonic trend: i.e., it increases initially, then decreases, and eventually rises slowly with increasing T_{in} and combustion temperature.

(2) Reactions within the Extended Zeldovich route play a crucial role in reducing the fuel-NO. In some operating conditions, the contribution of these reactions to the consumption of fuel NO can even reach 97 %. This explains why some previous studies (e.g. Ref. [28]) have mistakenly suggested that the thermal-NO had a negative contribution to the NO emission.

(3) The oxidations of N_2 and NH_3 are coupled, through semi-marked NN*O and N*N, with N*N being the dominant species, formed primarily by reactions R8 and R18.

(4) Across all combustion regimes and technologies examined in this study, fuel-NO consistently represents the dominant source of NO in pure ammonia combustion, contributing more than 75 % to the total NO emissions. In contrast, thermal-NO is negligible, accounting for less than 0.03 % of the total NO under typical conditions. Exceptions occur in cases involving oxygen-enriched combustion or flameless combustion at extremely high ambient or environmental temperatures, where the thermal-NO

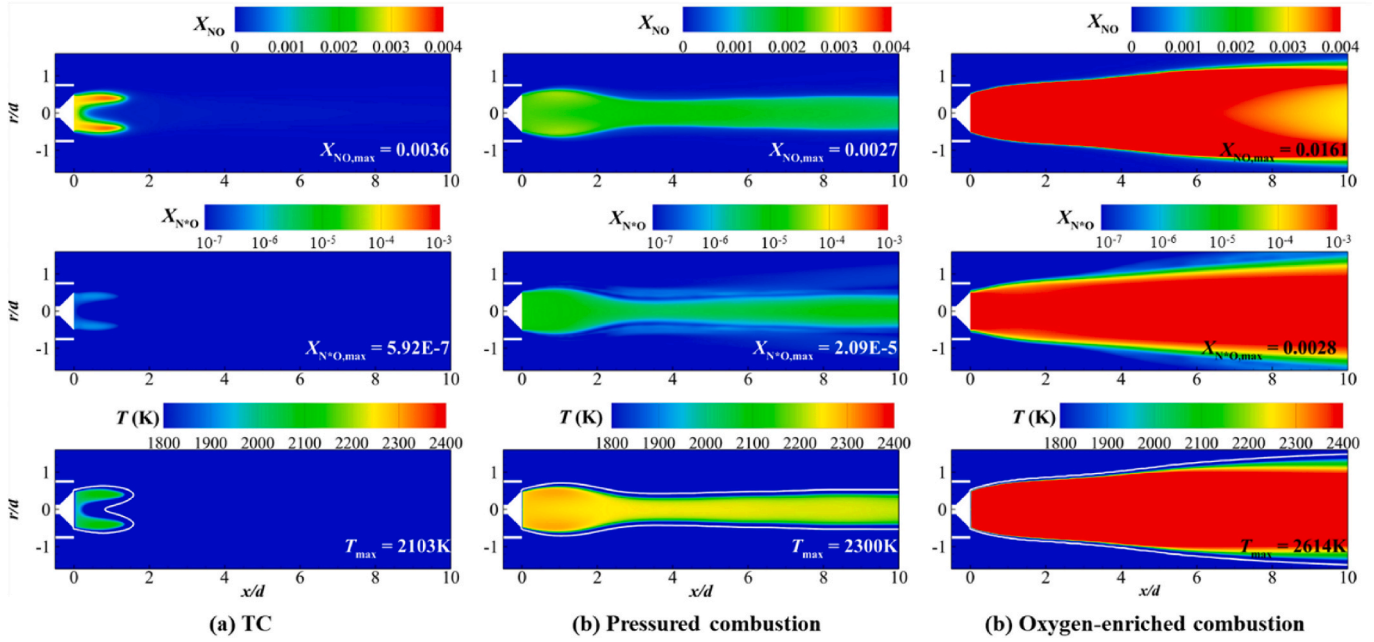

Fig. 10. Contours of the volume fractions of NO and N*O, along with the temperature field for the NH_3/air JHC flames at $\Phi = 1.0$: (a) normal TC (1.0 atm, $X_{O2,J} =$ 16.4 %), (b) pressured TC (10 atm, $X_{O2,J} = 16.4$ %), and (c) oxygen-enriched TC (1.0 atm, $X_{O2,J} = 30$ %). White lines represent the RZ boundaries.

contribution increases. Even in these scenarios, however, its share remains below 25 % of the total NO emissions.

CRediT authorship contribution statement

Xiangtao Liu: Writing – original draft, Visualization, Validation, Methodology, Investigation, Formal analysis, Data curation, Conceptualization. **Jicang Si:** Writing – review & editing, Resources, Conceptualization. **Guochang Wang:** Validation, Methodology, Investigation. **Mengwei Wu:** Validation, Formal analysis. **Jianchun Mi:** Writing – review & editing, Supervision, Software, Resources, Project administration, Conceptualization.

Declaration of competing interest

The authors declare that they have no known competing financial interests or personal relationships that could have appeared to influence the work reported in this paper.

Acknowledgments

This work is supported by the National Natural Science Foundation of China (No. 22350710788) and the Fundamental Research Funds for the Central Universities (No. 3132024218). The authors also acknowledge the support of the High-Performance Computing Platform of Peking University.

Data availability

Data will be made available on request.

References

[1] Chai WS, Bao Y, Jin P, Tang G, Zhou L. A review on ammonia, ammonia-hydrogen and ammonia-methane fuels. Renew Sustain Energy Rev 2021;147:111254.
[2] Berwal P, Kumar S, Khandelwal B. A comprehensive review on synthesis, chemical kinetics, and practical application of ammonia as future fuel for combustion. J Energy Inst 2021;99:273–98.
[3] Lang M, Su Y, Wang Y, Zhang Y, Wang B, Chen S. Experimental study on the effects of pilot injection strategy on combustion and emission characteristics of ammonia/diesel dual fuel engine under low load. Energy 2024;303(C).
[4] Mardani A, Oh SC, Kim H, Kim KC. Assessment on NOx formation for CH4/H2/NH3 flame under MILD condition: effect of air Swirl and ammonia fraction. Int J Hydrogen Energy 2024;80:1277–89.
[5] Shi C, Cheng T, Yang X, Zhang Z, Duan R, Li X. Implementation of various injection rate shapes in an ammonia/diesel dual-fuel engine with special emphasis on combustion and emissions characteristics. Energy 2024:132035.
[6] Wang Z, Zhang T, Wang D, Wang S, Ji C, Wang H, et al. A comparative study on the premixed ammonia/hydrogen/air combustion with spark ignition and turbulent jet ignition. Energy 2024;132814.
[7] Li Y, Feng L, Chen W. Chemical effect of H2 on NH3 combustion in an O2 environment via molecular dynamics simulations. Energy 2024:133026.
[8] Ariemma GB, Sabia P, Sorrentino G, Bozza P, de Joannon M, Ragucci R. Influence of water addition on MILD ammonia combustion performances and emissions. Proc Combust Inst 2021;38(4):5147–54.
[9] Shi G, Li P, Li K, Hu F, Liu Q, Zhou H, et al. Insight into NOx formation characteristics of ammonia oxidation in N2 and H2O atmospheres. Energy 2023;285:129412.
[10] Liang B, Gao W, Zhang K, Li Y. Ammonia-air combustion and explosion characteristics at elevated temperature and elevated pressure. Int J Hydrogen Energy 2023;48(53):20225–37.
[11] Li Z, Zhang Y, Zhang H. Kinetics modeling of NOx emission of oxygen-enriched and rich-lean-staged ammonia combustion under gas turbine conditions. Fuel 2024;355:129509.
[12] Wang Y, Sun J, Liu Q, Chen L, Gu M, Liu D, et al. NOx formation mechanism of plasma assisted ammonia combustion: a reactive molecular dynamics study. Energy 2024;293:130706.
[13] Péquin A, Evans MJ, Chinnici A, Medwell PR, Parente A. The reactor-based perspective on finite-rate chemistry in turbulent reacting flows: a review from traditional to low-emission combustion. Applications in Energy and Combustion Science 2023;16:100201.
[14] Tian J, Liu X, Shi H, Yao Y, Ni Z, Meng K, et al. Experimental study on MILD combustion of methane under non-preheated condition in a swirl combustion furnace. Appl Energy 2024;363:123109.
[15] Wang F, Li P, Mi J, Shu Z. A novel method to improve stability of MILD combustion in a highly heat-extracted furnace. Fuel 2021;292:120315.
[16] Mi J, Li P, Wang F, Cheong K-P, Wang G. Review on MILD combustion of gaseous fuel: its definition, ignition, evolution, and emissions. Energy Fuels 2021;35(9):7572–607.
[17] Sorrentino G, Sabia P, Bozza P, Ragucci R, de Joannon M. Low-NOx conversion of pure ammonia in a cyclonic burner under locally diluted and preheated conditions. Appl Energy 2019;254:113676.
[18] Xie M, Tu Y, Peng Q. Numerical study of NH3/CH4 MILD combustion with conjugate heat transfer model in a down-fired lab-scale furnace. Applications in Energy and Combustion Science 2023;14:100144.
[19] Liu X, Wang G, Si J, Li P, Wu M, Mi J. Distinct combustion characteristics of a one-dimensional premixed laminar flame of ammonia under various combustion regimes. Carbon Resources Conversion 2024;7(4):100229.
[20] Cafiero M, Sharma S, Kamal MM, Lubrano Lavadera M, Iavarone S, Coussement A, et al. Enhancing pure NH3 combustion: impacts of O2 enrichment under MILD conditions in a 20-kW semi-industrial scale furnace. Proc Combust Inst 2024;40(1–4):105336.

[21] Wang G, Liu X, Li P, Shi G, Cai X, Liu Z, et al. MILD combustion of a premixed NH3/air jet flame in hot coflow versus its CH4/air counterpart. Fuel 2024;355:129523.
[22] Park Y-K, Kim B-S. Catalytic removal of nitrogen oxides (NO, NO2, N2O) from ammonia-fueled combustion exhaust: a review of applicable technologies. Chem Eng J 2023;461:141958.
[23] Zhu X, Du J, Yu Z, Cheng Y-B, Wang Y. NOx emission and control in ammonia combustion: state-of-the-art review and future perspectives. Energy Fuels 2023;38(1):43–60.
[24] Zhao Z, Zhang T, Li X, Zhang L, Zhang Z, Chen Y, et al. NO formation mechanism of CH4/NH3 jet flames in hot co-flow under MILD-oxy condition: effects of co-flow CO2 and H2O. Fuel 2022;313:123030.
[25] Li J, Huang H, Kobayashi N, He Z, Nagai Y. Study on using hydrogen and ammonia as fuels: combustion characteristics and NOx formation. Int J Energy Res 2014;38(9):1214–23.
[26] Mohammadpour A, Mazaheri K, Alipoor A. Reaction zone characteristics, thermal performance and NOx/N2O emissions analyses of ammonia MILD combustion. Int J Hydrogen Energy 2022;47(48):21013–31.
[27] Wang G, Si J, Xu M, Mi J. MILD combustion versus conventional bluff-body flame of a premixed CH4/air jet in hot coflow. Energy 2019;187:115934.
[28] Liu X, Wang G, Wang F, Li P, Si J, Hanif F, et al. Classification and characteristics of ammonia combustion in well stirred reactor. Int J Hydrogen Energy 2024;55:1–13.
[29] Wu B, Wang Y, Wang D, Feng Y, Jin S. Generation mechanism and emission characteristics of N2O and NO in ammonia-diesel dual-fuel engine. Energy 2023;284:129291.
[30] Mi J, Li P, Dally BB, Craig RA. Importance of initial momentum rate and air-fuel premixing on moderate or intense low oxygen dilution (MILD) combustion in a recuperative furnace. Energy Fuels 2009;23(11):5349–56.
[31] Liu X, Wang G, Si J, Li P, Wu M, Mi J. MILD combustion characteristics of a premixed CH4/air jet flame in hot coflow from a bluff-body burner. Applications in Energy and Combustion Science 2024;19:100279.
[32] Kariuki J, Dawson JR, Mastorakos E. Measurements in turbulent premixed bluff body flames close to blow-off. Combust Flame 2012;159(8):2589–607.
[33] Jocher A, Evans MJ, Medwell PR, Dally BB, Pitsch H, Nathan GJ. On the use of oscillating jet flames in a coflow to develop soot models for practical applications. Proc Combust Inst 2021;38(1):1309–17.
[34] Li S, Liu X, Li Y, Si J. Identification of NOx formation based on nitrogen element labeled NH3 combustion. Electric Power Technology and Environmental Protection 2024;40(5):495–503.
[35] Kee R, Rupley FM, Millerm JA, Coltrin JA, Grcar JF, Meeks E. CHEMKIN collection, release 4.1. San Diego CA: Reaction Design Inc.; 2010.
[36] Zhang X, Moosakutty SP, Rajan RP, Younes M, Sarathy SM. Combustion chemistry of ammonia/hydrogen mixtures: jet-stirred reactor measurements and comprehensive kinetic modeling. Combust Flame 2021;234:111653.
[37] Bowman CT, Hanson RK, Davidson DF, Gardiner WC, Jr, Lissianski V, Smith GP, Golden DM, Frenklach M, Goldenberg M. http://www.me.berkeley.edu/gri_mech/.
[38] Li P, Wang F, Mi J, Dally BB, Mei Z, Zhang J, Parente A. Mechanisms of NO formation in MILD combustion of CH4/H2 fuel blends. Int J Hydrogen Energy 2014;39(33):19187–203.
[39] Ali G, Zhou Y. Numerical analysis of NOx formation mechanisms and emission characteristics with different types of reactants dilution during MILD combustion of methane and coke oven gas. Fuel 2022;309:122131.
[40] Karimi Motaalegh Mahalegi H, Mardani A. Structure of the ethanol spray flame under conventional and MILD conditions. Fuel 2022;321:124015.
[41] Lewandowski MT, Parente A, Pozorski J. Generalised Eddy Dissipation Concept for MILD combustion regime at low local Reynolds and Damköhler numbers. Part 1: model framework development. Fuel 2020;278:117743.
[42] Parente A, Malik MR, Contino F, Cuoci A, Dally BB. Extension of the Eddy Dissipation Concept for turbulence/chemistry interactions to MILD combustion. Fuel 2016;163:98–111.
[43] Chui E, Raithby G. Computation of radiant heat transfer on a nonorthogonal mesh using the finite-volume method. Numer Heat Tran 1993;23(3):269–88.
[44] Pope SB. Computationally efficient implementation of combustion chemistry using in situ adaptive tabulation. 1997.
[45] Liu X, Wang G, Si J, Wu M, Xu M, Mi J. On a premixed NH3/O2 jet flame in hot coflow of gaseous H2O versus N2. Int J Hydrogen Energy 2024;72:588–600.
[46] Lu T, Law CK. Toward accommodating realistic fuel chemistry in large-scale computations. Prog Energy Combust Sci 2009;35(2):192–215.
[47] Sabia P, Sorrentino G, Manna V, Ariemma GB, de Joannon M, Ragucci R. MILD combustion of ammonia, from kinetics to applications. In: Ammonia and hydrogen for green energy transition, vol. 9. Singapore: Springer Nature Singapore; 2024. p. 187–203.
[48] Li Z, Li S. Effects of inter-stage mixing on the NOx emission of staged ammonia combustion. Int J Hydrogen Energy 2022;47(16):9791–9.
[49] Malte P, Pratt D. The role of energy-releasing kinetics in NOx formation: fuel-lean, jet-stirred CO-air combustion. Combust Sci Technol 1974;9(5–6):221–31.
[50] Zhang M, An Z, Wei X, Wang J, Huang Z, Tan H. Emission analysis of the CH4/NH3/air co-firing fuels in a model combustor. Fuel 2021;291.
[51] Kiani M, Kohansal M, Masoumi S, Ashjaee M, Houshfar E. An experimental investigation on non-preheated MILD combustion of syngas/ammonia/air. J Therm Anal Calorim 2023;148(21):11783–97.
[52] Zhang J, Huang M, Tang B, Liu Z, Zhang H, Song Y, Fan X, Niu X. The impact of hydrogen addition and OH concentration on NO emissions in high-pressure NH3/air combustion. Int J Hydrogen Energy 2024;54:1017–28.
[53] Sabry Rashed E, Elwardany AE, Emam M, Abo-Elfadl S, Mori S, Hassan H. 3D numerical study of NH3/H2 MILD combustion in a reversed flow MILD combustion furnace. Appl Therm Eng 2024;252.
[54] Kobayashi H, Hayakawa A, Somarathne Kdkunkuma A, Okafor Ekenechukwu C. Science and technology of ammonia combustion. Proc Combust Inst 2019;37(1):109–33.